Journal of Zhejiang University-SCIENCE A 2025 26(11):1070-1082
www.jzus.zju.edu.cn; www.springer.com/journal/11582
E-mail: jzus_a@zju.edu.cn

Research Article
https://doi.org/10.1631/jzus.A2400513

Check for updates

Design and fabrication of biomimetic four-region drug-loaded cartilage scaffolds with porous hollow fibers

Yu CHEN[1,2*], Yuzhe MA[1,2*], Jianzhong FU[1,2], Xinhua YAO[1,2✉]

[1]*State Key Laboratory of Fluid Power and Mechatronic Systems, School of Mechanical Engineering, Zhejiang University, Hangzhou 310058, China*
[2]*Key Laboratory of 3D Printing Process and Equipment of Zhejiang Province, School of Mechanical Engineering, Zhejiang University, Hangzhou 310058, China*

Abstract: Articular cartilage, which plays a vital role in joint structure, is susceptible to damage from trauma and degenerative joint diseases. Traditional methods for cartilage treatment often involve complex surgical procedures with limited efficacy. Alternatively, implantable drug-loaded scaffolds are an increasingly attractive cartilage treatment option. To address the challenges of structural and functional compatibility between scaffolds and native cartilage, as well as issues related to drug loading, we design a novel cartilage scaffold with a four-region hollow porous fiber network structure. Using an extrusion-based 3D printing platform, a biphasic silicone ink composed primarily of liquid-phase silicone and solid particles was employed to construct the hollow porous fiber network. Mechanical compression tests demonstrate that the cartilage scaffold has mechanical characteristics similar to those of native cartilage tissue, and ultraviolet spectrophotometry measurements confirm its ability to control drug release. These results showcase the feasibility and effectiveness of the proposed cartilage substitute structure.

Key words: Bionic design; 3D printing; Cartilage scaffold; Gradient porous structure; Regulation of mechanical properties; Drug delivery systems

1 Introduction

Articular cartilage defects represent a serious medical issue, as they frequently result in severe disability for patients. Due to the extremely limited regenerative capacity of articular cartilage (Liu et al., 2018), its damage or degeneration can lead to chronic pain and functional impairment. Thus, developing effective clinical methods to treat cartilage injury is of paramount importance (Liu JX et al., 2019; Schizas et al., 2019). Among novel methods, implanting scaffolds at the injury site to mimic cartilage function has emerged as a promising treatment (Zhang et al., 2019; Hua et al., 2022; Shen et al., 2024; Yang HX et al., 2024; Yang SH et al., 2024). However, current scaffold implantation therapies face numerous challenges in clinical application, such as the need for complex surgical procedures (Kwon et al., 2019), significant immune rejection (Soleymani et al., 2024), mechanical property mismatch with native cartilage (Zhang et al., 2022), inadequate viscoelasticity, the limited unifunctional nature of certain scaffolds, and other factors. Therefore, despite recent advancements, scaffold implantation treatment leaves much to be desired. Its associated issues often result in treatment delays and subpar clinical outcomes compared to expectations.

Optimized cartilage scaffold design is imperative when replacing native cartilage to treat degenerative diseases (Liu JY et al., 2019; Malda et al., 2019; Kim et al., 2024; Singh et al., 2024). As understanding of native cartilage structure has advanced, cartilage scaffold design has progressed from simple monophasic models to more sophisticated biphasic, triphasic, and multiphasic constructs. These advancements aim to improve upon early designs, which failed to represent the complex structure of native cartilage. For instance, monophasic collagen scaffolds with radially aligned and randomly arranged collagen fibers were recently

✉ Xinhua YAO, yaoxinhuame@zju.edu.cn
* The two authors contributed equally to this work
Xinhua YAO, https://orcid.org/0000-0003-0261-3938

Received Nov. 10, 2024; Revision accepted Mar. 24, 2025;
Crosschecked Sept. 26, 2025; Online first Nov. 14, 2025

© Zhejiang University Press 2025

designed and fabricated (Chen et al., 2015). While these scaffolds have shown promise in promoting mesenchymal stem cell migration and healing in vitro, they do not replicate the full depth and functional complexity of native cartilage. Studies on mesenchymal stem cell migration (in vitro) and bone-cartilage defect repair (in vivo) have demonstrated that radially aligned collagen fiber scaffolds perform well in promoting cell migration and healing. Following 26 weeks of implantation in goats, comparative analyses between collagen/glucosamine biphasic scaffolds and polylactic/polyglycolic acid biphasic scaffolds in terms of morphology, histology, and mechanical properties revealed that the collagen/glucosamine biphasic scaffold was more effective in the treatment of degenerative cartilage disease (Getgood et al., 2012). However, while biphasic scaffolds help regenerate cartilage and bone layers, they fail to address the calcified cartilage region, which is a critical component for interface integration; this can lead to delamination between layers and failures in tissue repair. In another study using iterative freeze-drying technology, triphasic scaffolds based on hyaluronic acid, Type I collagen, and hydroxyapatite were prepared, with Type II collagen added in the middle and upper layers to mimic natural cartilage components (Levingstone et al., 2016a, 2016b). These scaffolds enabled long-term repair of goat articular cartilage, effectively simulating the hierarchical structure of the cartilage-bone interface. Nevertheless, this scaffold type still failed to achieve tight integration with the surrounding tissue.

Currently, gradient scaffolds are attracting increasing attention, as they more accurately mimic primary cartilage tissue and possess gradient chemical compositions and structural characteristics (Parisi et al., 2020; Wang WZ et al., 2024). For example, selective laser sintering technology was used to prepare a seven-layer gradient scaffold with poly(ε-caprolactone) (PCL) and hydroxyapatite microspheres as the substrate (Du et al., 2017). Additionally, the combination of PCL and hydrogel components such as methacrylated hyaluronic acid (MeHA) in scaffolds has been used to enhance angiogenesis and tissue regeneration in cell transplantation therapy (Yang HX et al., 2024). Moreover, arginine-glycine-aspartic acid-silk fibroin-DNA hydrogel-based microspheres (RSD-MSs) were developed to enhance cartilage repair, as they possess the potential to promote chondrogenic differentiation of bone marrow stem cells (BMSCs) and facilitate cartilage regeneration (Shen et al., 2024). Both in vitro and in vivo experiments have confirmed the role of scaffolds with complex structures or composite materials in promoting osteochondral repair and regeneration. However, such scaffolds still lack full biological functionality, with natural tissue integration and sustained biological activity remaining major limitations.

In recent years, cartilage scaffolds with varying chemical compositions and structural characteristics have been explored (Gui et al., 2023; Wang et al., 2024). However, monophasic scaffolds still fail to replicate the stratified structure of osteochondral units, which is essential for effective damage treatment and natural cartilage replacement. Although biphasic scaffolds have shown promise in promoting the regeneration of cartilage and bone layers, they often neglect the calcified cartilage region, which results in poor integration between the scaffold and cartilage. This can lead to delamination between layers and, ultimately, failed cartilage treatment (Da et al., 2013). Furthermore, the limited metabolic capacity of cartilage tissue hinders the development of strong bonds between the scaffold and natural tissue. Therefore, a major goal is to design scaffolds with inherent tissue integration capabilities, so as to ensure long-term functionality, stable biological fixation, and appropriate mechanical conduction following implantation (Pattnaik et al., 2023). Incorporating drug delivery systems into scaffolds promotes improved integration between the scaffold and the implant site, minimizes inflammation during healing, and extends the retention time of therapeutic agents, ensuring their sustained action at the damaged site (Kim et al., 2021; Han et al., 2023). However, research on biomimetic cartilage scaffolds that can simultaneously replicate the structure and biological functions of native cartilage remains in its infancy. To improve treatment of cartilage damage, it is crucial to develop scaffolds that both match the mechanical properties of native cartilage and integrate effective drug delivery systems.

To improve mechanical performance matching and drug-coordinated biological function in cartilage scaffolds (Wang MK et al., 2024; Yang SH et al., 2024), we propose a novel biomimetic four-region drug-loading porous cartilage scaffold structure. Addressing mechanical mismatch, a four-region biomimetic 3D fiber network structure with adjustable structural parameters was designed, inspired by the native four-region

architecture of cartilage. The fiber structure within each region of the cartilage scaffold differs in diameter, spacing, and arrangement. Utilizing extrusion-based 3D printing technology with controlled printing paths and process parameters, we achieved zonal construction and integration of the cartilage scaffold with effective matching to the mechanical properties of native cartilage. In the context of drug-coordinated treatment, the scaffold fibers were designed to be internally hollow and porous-walled. As water penetrates the scaffold, it dissolves the drug powder within the fiber walls, and the resulting solution is stored in the fiber tube pores. When the scaffold is compressed, drugs are slowly released under capillary action, thus achieving functionalities of loading and sustained release. The proposed biomimetic drug-loaded cartilage scaffold offers a novel therapeutic approach for degenerative cartilage diseases.

2 Materials and methods

2.1 Materials

A shear-thinning polydimethylsiloxane (PDMS) material, SE 1700, and a low-viscosity PDMS material, Sylgard 184, were sourced from Dow Corning (Auburn, USA). Sodium hydrogen carbonate ($NaHCO_3$), sodium chloride (NaCl), hydrochloric acid (HCl), ethanal, and toluene were acquired from Sinopharm (Beijing, China). Deionized water, cetyltrimethyl ammonium bromide (CTAB), tetraethyl orthosilicate (TEOS), (3-Aminopropyl) triethoxysilane (APTES), gallium (III) nitrate hydrate ($Ga(NO_3)_3 \cdot nH_2O$), rhodamine B, titanium chloride solution ($TiCl_3$), and 4-methyl-2-pentanone were sourced from Aladdin (Shanghai, China). All other chemicals and reagents used were of analytical grade and did not require further purification. Liquid nitrogen was sourced from Otterson (Zhejiang, China). Phosphate-buffered saline (PBS) and trypsin were acquired from Gibco (California, USA). Human chondrosarcoma cell lines SW 1353 and L-15 medium were obtained from Zhong Qiao Xin Zhou (Shanghai, China).

2.2 Ink preparation

Biphasic viscoelastic PDMS inks are prepared by blending two silicone elastomers in the liquid phase, SE 1700 and Sylgard 184 (which is used to dilute SE 1700 for appropriate rheological properties), and particles in the solid phase, NaCl and $NaHCO_3$ (which are used as pore-forming agents). Both SE 1700 and Sylgard 184 base materials are mixed with their curing agents in a 10:1 (base to curing agent) ratio by weight prior to blending. NaCl particles are ground with a planetary ball mill JX-2G (Jingxin, Shanghai, China) and sieved through a 150-mesh sieve before blending. The final inks are loaded into a 5-mL syringe barrel at room temperature and spun in a high-speed centrifuge TG16-WS (Cence, Hunan, China) at 5000 r/min for 5 min to remove air bubbles.

2.3 Preparation for 3D printing

The 3D printing is performed using a BP6601 3D bioprinter (EFL, Suzhou, China) with an in-situ curing device. The biphasic viscoelastic PDMS inks are loaded into 5-mL syringe barrels at room temperature, which are then capped with co-axial nozzles. The co-axial nozzles are equipped with an 18GA (Φ850 μm) outer nozzle and a 28GA (170 μm) inner nozzle, which is blocked with a solid pin. A unit with a built-in air pump is used to control the extrusion pressure. The printing speed is managed with a program (G-code) that is sent to the printer using Repetier software. The parameters of the 3D printing process are shown in Table 1.

Table 1 Extrusion 3D printing process parameters

Parameter	Value
Extrusion pressure (kPa)	160
In-situ curing temperature (℃)	160
Printing speed (mm/s)	1.8
First-layer height (mm)	1.3
Interlayer height (mm)	1.2

2.4 Preparation of the biomimetic four-region drug-laden porous cartilage scaffold

Overall, the scaffold has a hollow fiber network structure, which can be divided into four regions from bottom to top: a shallow region structure with relatively small fiber diameter and cross-arranged fibers, a transition region structure with many diagonal fibers with relatively large fiber diameter, a radial region structure with the largest-diameter cross-arranged fibers, and a calcified cartilage region with dense fibers. Each four-region drug-loaded porous cartilage scaffold was fabricated through 3D printing and in-situ curing

using biphasic silicone ink. Then, pore-forming agents such as sodium chloride and sodium bicarbonate were removed through placement in a water bath. The final scaffolds were obtained after drying in a 40 ℃ chamber for 20 min.

2.5 Simulation of the cartilage scaffold structure

We developed numerical models for the compressional mechanical properties of the cartilage scaffolds, so as to determine optimal structural design parameters, including fiber diameter, fiber distance, and fiber arrangement angle. The simulations were 3D finite-element models in COMSOL Multiphysics 6.0. Mooney-Rivlin constitutive model parameters for hyperelastic materials were fit to uniaxial tensile data from the type II dumbbell PDMS standard specimen. Fixed constraints were applied to the bottom surface of the geometric model in the negative z-direction, with displacement along this direction being specified at the opposite end of the model. No additional settings were required for the other surfaces. The constitutive parameters of the Mooney-Rivlin models were C_{10}=46617 Pa, C_{01}=3.0974×10^5 Pa, and D_1=1.2861×10^{-6} Pa. Here, C_{10} and C_{01} are the material constants that define the nonlinear elastic behavior of the material, and D_1 represents the damping parameter that characterizes the rate-dependent behavior or viscosity in the material model. Scaffold samples with different structural design parameters were then modeled through orthogonal experiment design.

2.6 Surface topography and porosity

A cartilage scaffold sample was printed for morphological observations and porosity evaluation, with an overall size of 8 mm×8 mm×15 mm. The printed sample was placed in a water bath and heated until boiling, such that solid particles and holes were removed by the water. A front image of the cartilage scaffold sample was captured by a macro camera, and then the cross-section of the empty fiber structure was imaged using a scanning electron microscope (SEM; Zeiss, Germany). The threshold segmentation function in the ImageJ software was used to screen the pore region, measure the total number of pixels in the pore region, and calculate its porosity (φ_P) according to the following formula:

$$\varphi_P = \frac{A_P}{A_{all}} \times 100\%, \tag{1}$$

where A_P is the area of pores in the cross-section, and A_{all} is the area of the cross-section.

2.7 Mechanical properties

A uniaxial compression test is performed to obtain the stress–strain curve, and thus verify the validity of the simulation model in characterizing the mechanical properties of the scaffolds. The mechanical properties of the designed cartilage scaffold are mainly related to three structural parameters: fiber diameter, fiber spacing, and fiber arrangement direction. In order to explore the influence of various parameters on the mechanical properties of cartilage scaffolds, 25 groups of simulation analysis models were constructed according to the mixed horizontal orthogonal tests of one factor, three levels, two factors, five levels, and the pseudo-horizontal method (Fig. 1). The initial length and width of each sample were first measured, and the cross-sectional area of the scaffold was calculated. Then, a preload was slowly applied to the sample. The compression rate was set to 10 mm/min. After the scaffold was compressed to 20% of its original length, the compression

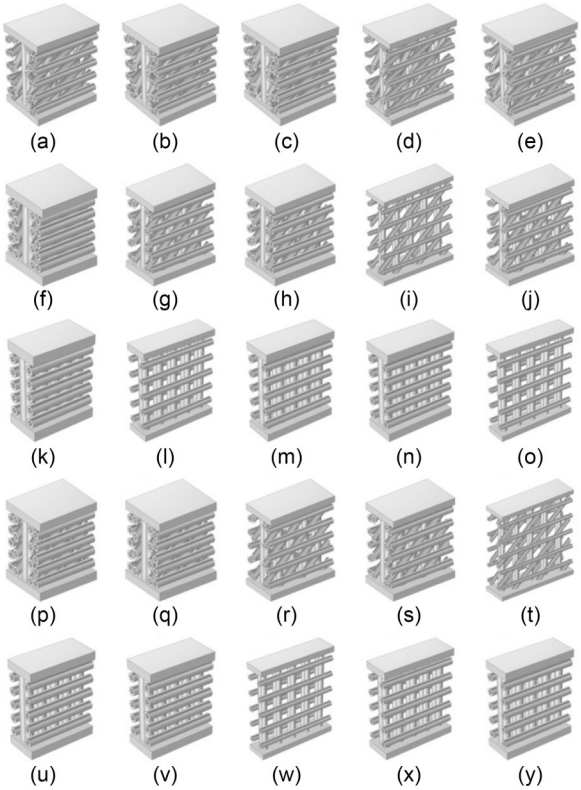

Fig. 1 COMSOL Multiphysics parametric geometric modeling. Figs. 1a–1y correspond to sequences 1–25 in Table 4, respectively

modulus was estimated using the slope of the initial linear region of the stress–strain curve.

2.8 Sustained drug release properties

A gallium complexing compound was first produced through the reaction of gallium nitrate solution with rhodamine B in acidic conditions. Then, the standard curve of the gallium complexing compound was measured under the maximum absorption peak using a ultraviolet (UV) spectrophotometer (Shimadzu, Japan). The scaffolds were submerged in 20 mL of deionized water, then simultaneously, 5 mL of gallium (III) nitrate sustained-release solution was extracted, and 5 mL of deionized water was replenished. These samples of solution were extracted at times of 1, 2, 4, 6, 8, 12, 24, 48, and 72 h in 0%, 5%, 10%, 15%, and 20% compression conditions. Subsequently, samples were reacted with rhodamine B in acidic conditions to obtain the gallium complexing compound. Then, the absorbance of each gallium complexing compound was measured by the UV spectrophotometer at the maximum absorption peak. Finally, the concentration of gallium (III) nitrate was determined based on the standard premeasured curve (Zhou et al., 2005). The cumulative release percentage of gallium (III) nitrate (p_n) was calculated by:

$$p_n=\frac{c_n v_n+\sum_{i=1}^{n} c_i v_i o_i}{m}\times 100\%, \tag{2}$$

where c_n is the concentration of gallium (III) nitrate in sample n, v_n is the residual volume of deionized water in sample n, c_i is the concentration of gallium (III) nitrate in sample i, v_i is the extracted volume in sample i, o_i is the dilution ratio of the solution in sample i, and m is the mass of gallium (III) nitrate.

2.9 Cytocompatibility evaluation

2.9.1 Cell culture

SW1353 was cultured in an L15 medium (Leibovitz) supplemented with 10% fetal bovine serum (Gibco, USA) and a 1% penicillin-streptomycin formulation (Gibco, USA) at 37 °C with 5% CO_2.

2.9.2 Cytocompatibility test

SW1353 was cultured on the scaffold for 48 h before the biocompatibility test. The cytotoxicity of the scaffolds under different treatments was then measured using a Calcein-AM (Calcein acetoxymethyl ester)/PI (propidium iodide) viability/cytotoxicity kit (Solarbio, Beijing, China) according to the manufacturer's protocol.

2.9.3 Statistical analysis

Statistical analysis was performed using OriginPro 9.1 and GraphPad Prism 8.0. All experiments involved at least triplicate samples, and the data were presented with the mean and standard deviation (SD). Two-sided $p<0.05$ was used as the criterion for statistical significance.

3 Results and discussion

3.1 Bionic design method and manufacturing process of the cartilage scaffold

Articular cartilage is a special connective tissue that covers the ends of joints. Its smoothness and wear-resistance enable it to slide and absorb impact forces when a joint moves slightly, enabling the joint to withstand high cyclic loads (Gu et al., 2023). Articular cartilage consists mainly of sparse chondrocyte populations embedded in a broad extracellular matrix (Sun et al., 2020). The unique biological and biomechanical properties of articular cartilage are intrinsically linked to its structure and composition, as well as to the interactions between chondrocytes and the extracellular matrix. Morphologically, mature articular cartilage can be divided into four distinct regions from shallow to deep. The superficial layer consists of thin and dense collagen fibers, which are mainly used to resist tensile stress. The transitional layer is composed of diagonal collagen fibers of large diameter and is mainly responsible for bearing compressive stress. The radial layer is composed of the largest-diameter collagen fibers and also acts to resist compressive stress. Finally, the calcified cartilage region is characterized by thick and densely arranged collagen fibers, whose function is to anchor the cartilage to the underlying bone.

To enable cartilage scaffolds to replicate the mechanical function of natural cartilage and facilitate synergistic treatment through slow drug release, the proposed scaffold structure is that of a 3D network composed of hollow porous fibers stacked at a certain angle. The four-region structure of the cartilage scaffold mimics natural cartilage and can be divided into

four regions: the superficial region, transitional region, radial region, and calcified cartilage region (Fig. 2a). The structural parameters of each region are closely related to their mechanical properties. Through path planning and parameter adjustment for the 3D printing, four regions of the scaffold were manufactured with different structural parameters (Fig. 2a). During the preparation of the cartilage scaffolds, gallium nitrate powder was embedded into the fibrous wall of the scaffold. After implantation, water in the body flows through the hollow fiber tube due to "capillary effects" (Li et al., 2021). The gallium nitrate particles embedded in the fiber wall dissolve in the gallium ion water solution and are stored in the pores of the tube wall. When the scaffold is compressed, the scaffold slowly releases gallium nitrate solution instead of discharging it all at once due to the "capillary effect" (Cai et al., 2022). Therefore, this structure enables the proposed cartilage scaffold to facilitate long-term drug release and match the mechanical functions of natural cartilage, thereby improving treatment efficacy (Fig. 2a). A macroscopic image of the scaffold and an SEM image of a single hollow porous fiber (Fig. 2b) showcase the hollow structure. Notably, after the pore-forming agent was removed during the water bath, it was observed that the particles formed different pore sizes. The porosity (φ_P) calculated from Eq. (1) was 60.19%, thus providing ample space for cell growth and drug release.

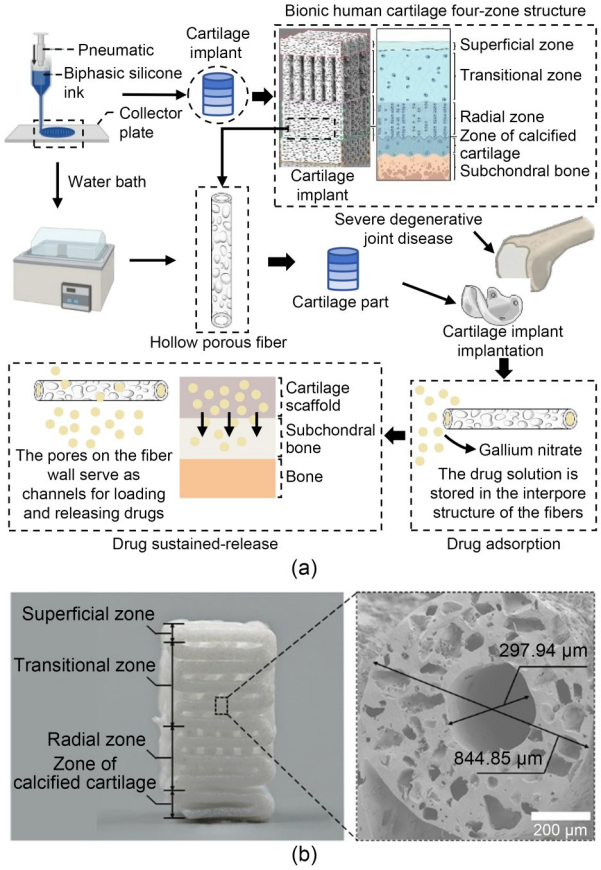

Fig. 2 Bionic design and fabrication of cartilage scaffold structure: (a) bionic four-region drug-loaded porous cartilage scaffold; (b) morphological characteristics of the bionic four-region drug-loaded porous cartilage scaffolds

3.2 3D printing equipment modification and performance study of biphasic silicone ink

The printing equipment was equipped with a coaxial nozzle with a solid needle structure and an in-situ curing device (Fig. 3a) to enable molding of the hollow fiber. The apparatus employs two nozzles with different coaxialities and diameters, and is formed into a core-shell structure through welding. Among these, the small-diameter nozzle in the inner layer has a plugged hollow portion to form a solid needle-like structure. The outer nozzle model has an inner diameter of 0.85 mm and an outer diameter of 1.25 mm; the inner nozzle model is 28G, and has an inner diameter of 0.17 mm and an outer diameter of 0.32 mm. The hollow fiber faces difficulties in forming when the biphasic silicone ink is printed at room temperature, and so intermediate collapse may occur in the hollow fiber, leading to low final molding quality. To avoid this, the in-situ curing device provides a high-temperature environment for the biphasic silicone ink printing, which promotes rapid in-situ curing and supports the integrity of the structural molding. The in-situ curing device adopts a positive temperature coefficient (PTC) heater, which is composed of ceramic heating elements and aluminum tubing. Its working voltage is 220 V, its rated power is 600 W, and its overall dimensions are 170 mm×140 mm×30 mm. The pressure control unit of the built-in air pump is used to control the extrusion pressure.

The effects of various components in the biphasic silicone ink on its viscosity, shear stress, storage modulus, loss modulus, and thixotropy were investigated, and an optimized formulation of the ink for subsequent printing experiments was determined (Table 2). Additional methods and data regarding this investigation are provided in the electronic supplementary materials (ESM).

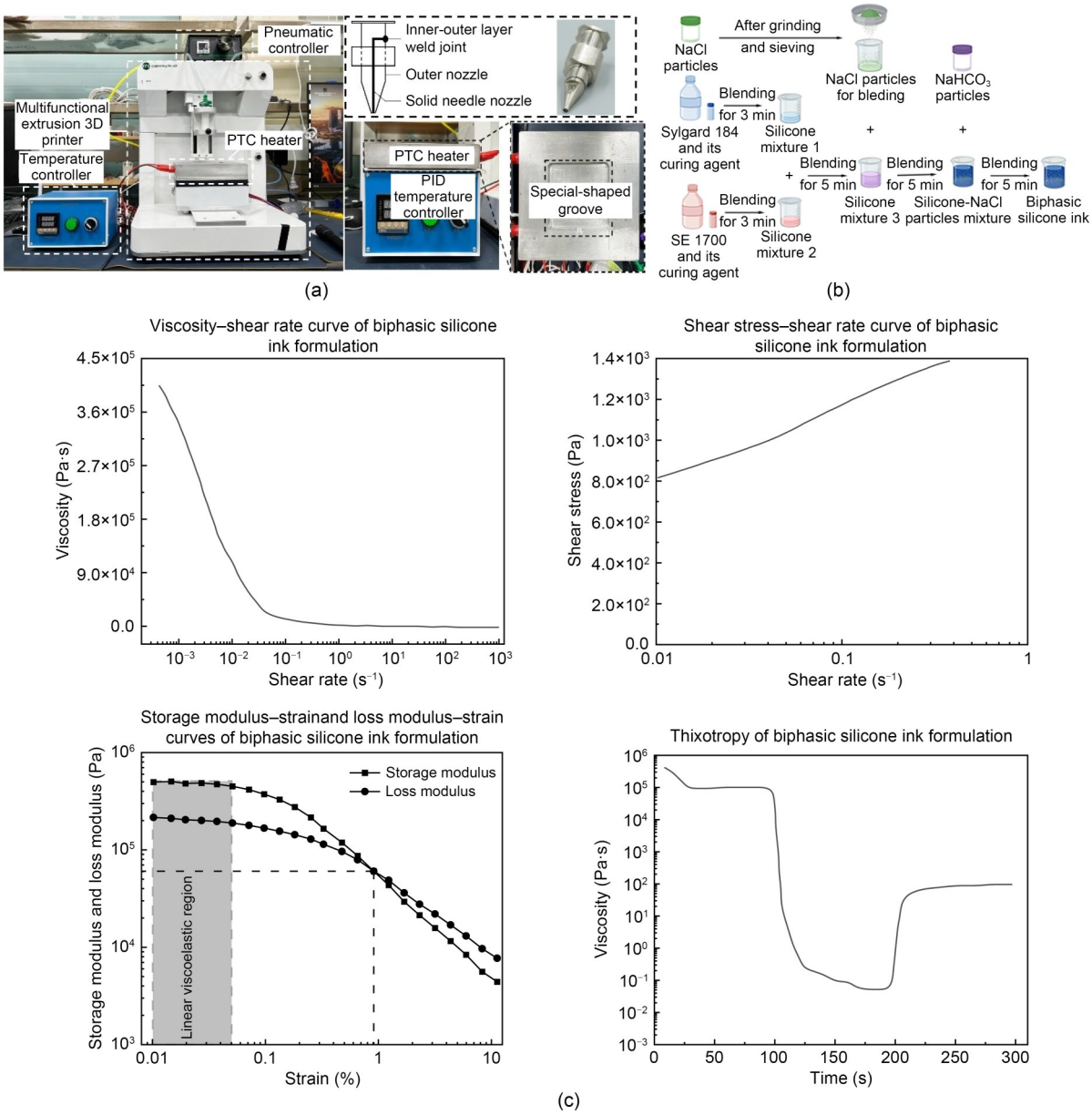

Fig. 3 Bionic design and fabrication of the cartilage scaffold structure: (a) 3D printing equipment; (b) preparation process of biphasic silicone ink; (c) rheological properties of the biphasic silicone ink formulation. PID is the proportional-integral-derivative; PTC is the positive temperature coefficient

Table 2 Composition and content of the biphasic silicone ink

Mass ratio of Sylgard 184 to SE 1700	Average particle size of NaCl particles (μm)	Total solid particle content (%)
1:9	104.40	100

The preparation process of the biphasic silicone ink is illustrated in Fig. 3b. The relevant rheological properties of this custom-formulated ink were tested, with the results shown in Table 3 and Fig. 3c. Overall, the biphasic silicone ink has high viscosity, strong non-Newtonian effects, and a robust ability to maintain its own form, thus meeting the requirements of subsequent printing experiments.

3.3 Mechanical property control of the cartilage scaffold

To analyze the mechanical compatibility between the cartilage scaffold and natural cartilage, the mechanical properties of the designed cartilage scaffold are

Table 3 Rheological properties of the biphasic silicone ink

Consistency coefficient[1]	n[2]	Yield stress (Pa)	tanδ[3]
1252.56	0.0304	819.33	0.4346

(1) The consistency coefficient is used to evaluate the viscosity; the higher the value, the greater the viscosity. (2) n is the flow index, and the value of n is used to quantify the non-Newtonian behavior of the fluid. The larger the value of $||n|-1|$, the stronger the non-Newtonian behavior of the tested fluid, which is characterized by more pronounced shear thinning. (3) The loss factor is defined as the ratio of energy dissipated and stored per cycle, which is used to characterize the viscoelastic properties of the material, and is given by $\tan\delta=G''/G'$, where G' and G'' are the energy storage modulus and energy dissipation modulus of the biphasic silicone ink, respectively

studied in terms of three main structural parameters: fiber arrangement angle, fiber distance, and fiber diameter (Fig. 4a). To investigate the impact of each parameter on the mechanical properties of the cartilage scaffold, 25 simulation models were established using a mixed-level orthogonal experimental design, with one-factor three levels and two-factor five levels combined using the quasi-level method. Table 4 presents the scaffold model structural parameters and simulated compression modulus (E) results from the orthogonal experiment. Figs. 1a–1y correspond to sequences 1–25 in Table 4. During compression, the fiber layers parallel to the stress direction initially serve as the primary stress units until they are crushed, at which point the primary stress units become the fiber layers which are oriented at an angle to the stress direction.

The orthogonal experiments yielded stress–strain curves for 25 simulated models (Fig. 4b). From these curves, it is evident that the stress–strain relationships for groups 5, 10, and 18 show gradually increasing trends—a phenomenon which is attributed to the specific angles of the fiber layers relative to the stress direction. The structural parameter–average compression modulus curves (Fig. 4c) indicate that the average compression modulus increases with fiber placement angle and fiber diameter, but decreases with fiber distance. The influences of fiber diameter, fiber distance, and fiber arrangement angle on the average compression modulus were revealed as representing primary and secondary factors. The area of the shaded regions in Fig. 4a is used to determine the hierarchical relationship between the three structural parameters, which can also be assessed using the range values in Table 5. The larger the shaded area (or the greater the range values), the more dominant the structural parameter. Thus, the three structural parameters, ranked from primary to secondary, are fiber diameter, fiber distance, and fiber arrangement angle. When the fiber arrangement angle is 90°, the fiber distance is 0.4 mm, and the fiber diameter is 1.2 mm, the compression modulus is at a maximum. These structural parameters are then plugged into the model, and the corresponding compression modulus is obtained. Fig. 4d shows the stress–strain curve of the simulation with the structural parameters corresponding to the maximum compression modulus. The compression modulus is 0.6553 MPa, which significantly exceeds the compression modulus of each group in Table 4.

Mechanical performance tests of the actual cartilage scaffold validated these simulation results. Within a small strain range of 0%–20%, a comparison of the real and simulated stress–strain curves (Fig. 4e) reveals approximate linear behavior. The trend of the actual stress–strain curves aligns well with the simulations. The real compression modulus (E_a) was calculated as 0.6789 MPa. The discrepancy between the actual and simulated compression moduli is less than 5%, confirming the validity and accuracy of the established simulation.

To ensure that the designed cartilage scaffold exhibits structural and functional compatibility with native cartilage tissue, ideal structural parameters for the scaffold were determined through simulation of the mechanical parameters and functions of various regions of native cartilage. It was determined that the superficial region should have the smallest fiber diameter, with vertically crossed fibers. The transitional region should possess relatively large fiber diameters and a substantial number of diagonal fibers so as to resist compressive stresses, with its compression modulus being second only to that of the radial region. The radial region should feature vertically aligned coarse fibers, as this is the primary structure for resisting compressive stress and must have the highest compression modulus. The calcified cartilage region should form a relatively dense structure. Table 6 details the structural parameters for each region of the four-region drug-loaded integrated porous cartilage scaffold.

The true stress–strain curves of the cartilage scaffold samples, printed according to the structural parameters in Table 4 (Fig. 4f), demonstrate that within a large strain range of 0%–80%, stress is positively and nonlinearly correlated with strain. Within a small strain range of 0%–20%, the stress–strain curves are

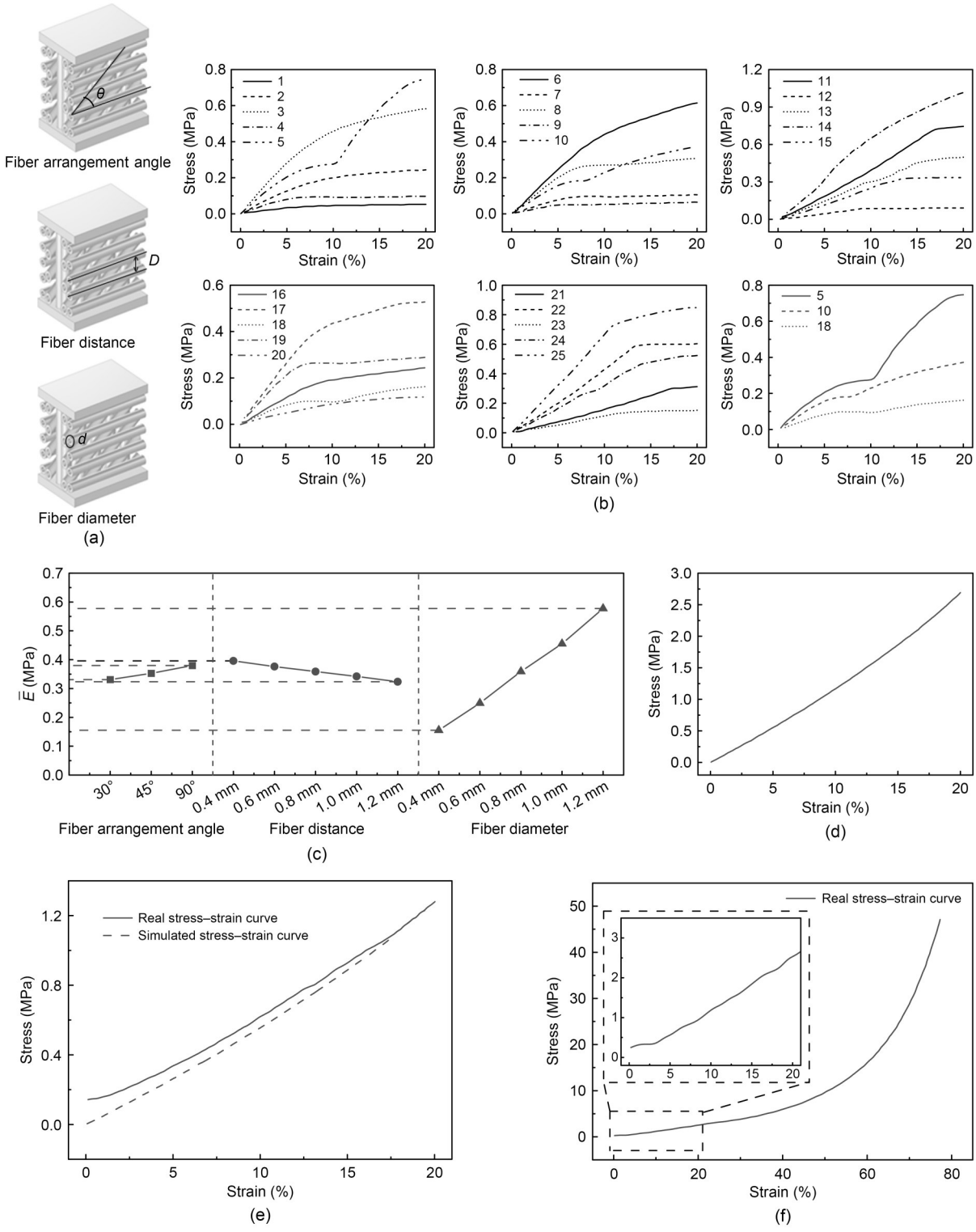

Fig. 4 Mechanical properties of the cartilage scaffold: (a) three main structural parameters affecting the mechanical properties of the cartilage scaffolds; (b) stress–strain curves of 25 groups of simulated cartilage scaffolds; (c) simulated average compression modulus corresponding to each level of the three factors in the cartilage scaffold structural design; (d) simulated stress–strain curve corresponding to the horizontal combination with the largest compression modulus; (e) comparison between the real stress–strain curve and the simulated stress–strain curve; (f) real stress–strain curve of the bionic four-region drug-loaded porous cartilage scaffold

Table 4 Structural parameters and simulated results on the cartilage scaffold structure

Sequence	Fiber arrangement angle (°)	Fiber distance (mm)	Fiber diameter (mm)	Compression modulus, E (MPa)
1	30	0.4	0.4	0.1585
2	30	0.6	0.8	0.3612
3	30	0.8	1.2	0.5633
4	30	1.0	0.6	0.1987
5	30	1.2	1.0	0.3741
6	45	0.4	1.2	0.6094
7	45	0.6	0.6	0.2542
8	45	0.8	1.0	0.4469
9	45	1.0	0.4	0.1377
10	45	1.2	0.8	0.3153
11	90	0.4	1.0	0.5310
12	90	0.6	0.4	0.1800
13	90	0.8	0.8	0.3665
14	90	1.0	1.2	0.5852
15	90	1.2	0.6	0.2602
16	45	0.4	0.8	0.3874
17	45	0.6	1.2	0.5861
18	45	0.8	0.6	0.2413
19	45	1.0	1.0	0.4240
20	45	1.2	0.4	0.1249
21	90	0.4	0.6	0.2932
22	90	0.6	1.0	0.4998
23	90	0.8	0.4	0.1748
24	90	1.0	0.8	0.3646
25	90	1.2	1.2	0.5433
$\overline{E}_{1-5}$	0.3311	0.3959	0.1552	
$\overline{E}_{6-10}$	0.3527	0.3763	0.2495	
$\overline{E}_{11-15}$	0.3846	0.3586	0.3590	
$\overline{E}_{16-20}$	0.3527	0.3420	0.4551	
$\overline{E}_{21-25}$	0.3751	0.3235	0.5774	
R	0.0534	0.0723	0.4223	

$\overline{E}_{1-5}$, $\overline{E}_{6-10}$, $\overline{E}_{11-15}$, $\overline{E}_{16-20}$, and $\overline{E}_{21-25}$ are the average values of compression moduli of sequences 1–5, 6–10, 11–15, 16–20, and 21–25, respectively, and R represents ranges of average compression moduli for fiber arrangement angle, fiber distance, and fiber diameter

Table 5 Mechanical properties of articular cartilage

Compression modulus (MPa)	Young's modulus (MPa)	Poisson's ratio
0.24–0.85	5–25	0.06–0.30

approximately linear. The actual compression modulus (E_b) was calculated as 0.8291 MPa, falling within the range of joint cartilage as shown in Table 5. The results show that the bionic four-region cartilage scaffold matches well with native cartilage in terms of mechanical properties, and might therefore effectively replace cartilage in this regard.

Table 6 Structural parameters of the four-region biomimetic drug-loaded cartilage scaffold ink

Region	Region proportion (%)	Fiber diameter (mm)	Fiber distance (mm)	Fiber arrangement angle (°)
Superficial region	10	0.8	0.4	90
Transitional region	40	1.0	0.4	45
Radial region	30	1.2	0.4	90
Calcified cartilage region	20	1.2	0.2	0

3.4 Characterization of drug loading, sustained drug release performance, and biocompatibility of the cartilage scaffold

In order to characterize the drug release performance of the cartilage scaffold, a compression experiment on the scaffold was designed to simulate the environment of in-vivo implantation. The drug release performance was characterized by measuring the content of gallium nitrate in the solution following the compression test, and calculating the cumulative release percentage of gallium nitrate for each measurement. A UV spectrophotometer was used to determine the concentration of gallium nitrate. Because gallium nitrate solution reacts with rhodamine B under acidic conditions, there is a maximum absorption peak in the UV spectrum when scanned by the spectrophotometer, and the standard curve measured under this maximum absorption peak has a clear linear relationship. Therefore, the concentration of gallium nitrate can be evaluated according to the concentration of the gallium (III) nitrate complex, in order to characterize the drug-loading and slow-release performance of the scaffold. The maximum absorption peak of the complex was 556 nm, as measured by full-spectrum scanning with the UV spectrophotometer. According to the standard curve of gallium (III) nitrate complex (Fig. 5a), the regression equation for gallium (III) nitrate complex is y=0.7755x+0.001683, and the correlation coefficient R^2 is 0.99948. These results reveal that the concentration of gallium (III) nitrate complex has a clear

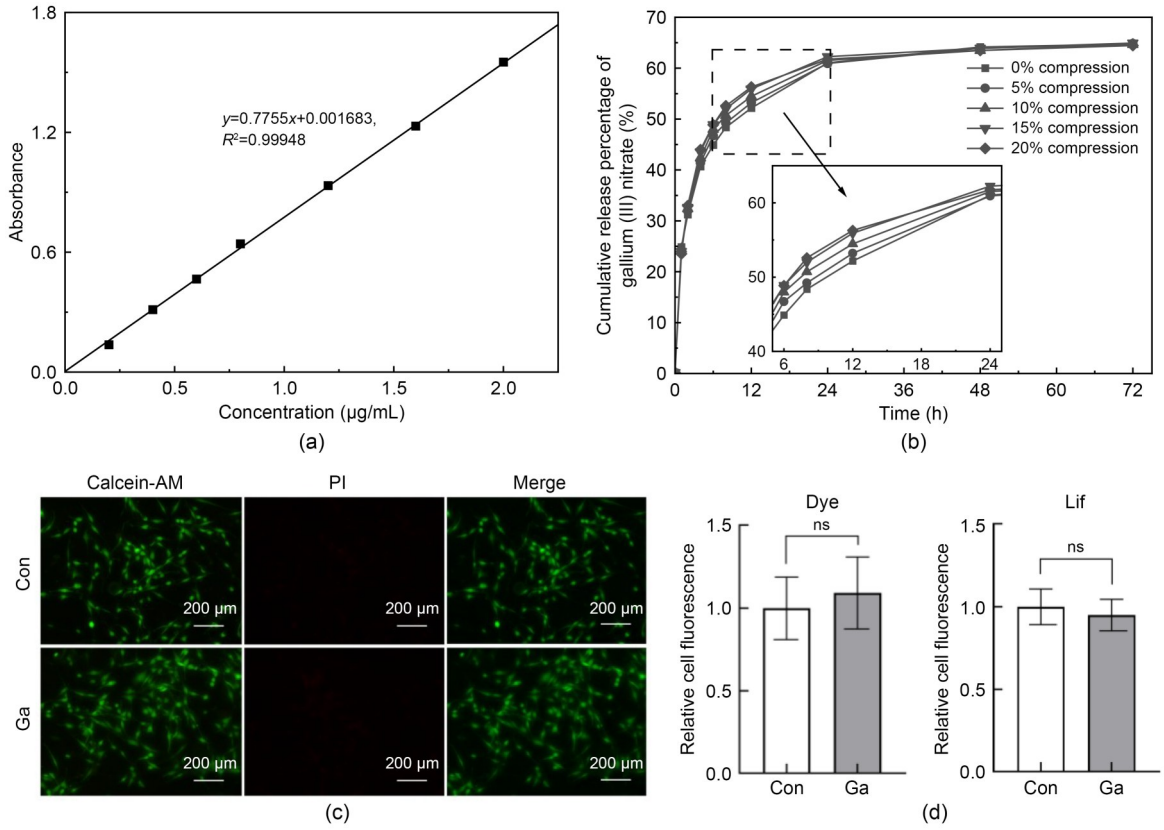

Fig. 5 Characterization of drug loading, sustained drug release performance, and biocompatibility of the cartilage scaffold: (a) standard curve of gallium (III) nitrate complex at the maximum absorption peak; (b) time curve of cumulative percentage release of gallium (III) nitrate; (c) live/dead staining fluorescence microscope images of human chondrosarcoma cells cultured on a cartilage scaffold for 48 h (Con refers to control group); (d) proliferation of chondrocyte on Ga-ion-carrying cartilage scaffold. Error bars represent standard deviations, and significant differences were assessed with Student's *t*-test; *$P<0.05$. Dye represents the relative fluorescence of dead cells, Lif represents the relative fluorescence of live cells, and ns indicates the absence of statistically significant difference

linear relationship with absorbance in the range of 0.2–2.0 μg/mL.

We next conducted compression experiments at various rates to evaluate the drug release performance of the scaffold under different compression conditions. The experimental results demonstrated that gallium (III) nitrate in the scaffold was gradually released at a high rate to a level of about 50% within 0–8 h, and then the release rate gradually decreased until 72 h, where the maximum cumulative release rate remained at approximately 65%. This indicates that the scaffold's drug release functionality is relatively stable, enabling rapid release to a desired concentration and maintenance of this concentration for a certain period. As the amount of compression increases, the rate of drug release gradually increases, and the time required to reach the maximum cumulative release percentage decreases. Moreover, no matter how the compression amount changes, the maximum cumulative release percentage remains stable. This phenomenon reflects the stability of the scaffold's drug release functionality, since slight deformation does not significantly alter the drug release effects.

To determine whether gallium nitrate-bearing scaffolds negatively impact normal cartilage cells during drug release, we performed cytotoxicity tests on the surface of porous materials containing gallium ions, and on control materials of the same shape (without gallium ions). As shown in Fig. 5c, after 48 h of culturing of human chondrosarcoma cells on cartilage scaffold samples, living cells showed green fluorescence under Calcein-AM staining, while dead cells showed red fluorescence under PI staining. Cell survival on the cartilage scaffold sample surfaces was high, regardless of the presence or absence of gallium nitrate, indicating that scaffolds containing gallium nitrate

have similarly small cytotoxicity compared to scaffolds without gallium nitrate.

4 Conclusions

In this study, a novel biomimetic four-region drug-laden porous cartilage scaffold was developed for the treatment of cartilage defects. To achieve structural and functional compatibility with native cartilage, the scaffold was designed with a biomimetic hollow porous fiber network with optimized structural parameters. The ideal structural parameters were determined through parameter–stress simulations. The scaffold's morphology was examined using SEM, revealing a porosity of 60.19%. Additionally, the compression modulus of the designed cartilage scaffold (E=0.8291 MPa) was found to closely match that of native cartilage tissue. In-vitro drug release performance was assessed using UV spectrophotometry, and revealed a trend of initial rapid release followed by sustained concentration; moreover, minor scaffold deformations were found not to significantly impact the drug release effects. Finally, the scaffold's biocompatibility was evaluated by placing human chondrosarcoma cells (SW 1353) on the scaffold surface and conducting live/dead assays. The findings indicated that the scaffold had no negative effects on the human chondrosarcoma cells. Through a comprehensive analysis of varying performance characteristics, the feasibility and effectiveness of the proposed biomimetic four-region drug-loaded porous cartilage scaffold were demonstrated.

Although the experimental results showcase the considerable potential of the scaffold for cartilage treatment, several key challenges must be addressed prior to clinical application. Improved scaling of production is critical for clinical application, since the scaffolds would need to be produced in sufficient quantity and with consistent quality. Also, it should be noted that the biomimetic design of the studied cartilage scaffolds primarily focused on mechanical properties and drug delivery. To better mimic native cartilage, additional complex functions such as wear resistance, buffering, and lubrication need to be incorporated. Therefore, scaffolds that achieve effective mechanical performance and biological functionality must also undergo rigorous in-vivo evaluations to assess their long-term biocompatibility, stability, and efficacy.

Acknowledgments

This work is supported by the National Natural Science Foundation of China (No. 52175278).

Author contributions

Yu CHEN designed the research. Yu CHEN and Yuzhe MA processed the corresponding data and wrote the first draft of the manuscript. Jianzhong FU helped to organize the manuscript. Xinhua YAO revised and edited the final version.

Declaration of interests

Yu CHEN, Yuzhe MA, Jianzhong FU, and Xinhua YAO declare no competing interests.

Data availability

The data that support the findings of this study are available from the corresponding author upon reasonable request.

References

Cai JC, Chen Y, Liu Y, et al., 2022. Capillary imbibition and flow of wetting liquid in irregular capillaries: a 100-year review. *Advances in Colloid and Interface Science*, 304: 102654. https://doi.org/10.1016/j.cis.2022.102654

Chen PF, Tao JD, Zhu SA, et al., 2015. Radially oriented collagen scaffold with SDF-1 promotes osteochondral repair by facilitating cell homing. *Biomaterials*, 39:114-123. https://doi.org/10.1016/j.biomaterials.2014.10.049

Da H, Jia SJ, Meng GL, et al., 2013. The impact of compact layer in biphasic scaffold on osteochondral tissue engineering. *PLoS One*, 8(1):e54838. https://doi.org/10.1371/journal.pone.0054838

Du YY, Liu HM, Yang Q, et al., 2017. Selective laser sintering scaffold with hierarchical architecture and gradient composition for osteochondral repair in rabbits. *Biomaterials*, 137:37-48. https://doi.org/10.1016/j.biomaterials.2017.05.021

Getgood AMJ, Kew SJ, Brooks R, et al., 2012. Evaluation of early-stage osteochondral defect repair using a biphasic scaffold based on a collagen-glycosaminoglycan biopolymer in a caprine model. *The Knee*, 19(4):422-430. https://doi.org/10.1016/j.knee.2011.03.011

Gu ZH, Wang JY, Fu Y, et al., 2023. Smart biomaterials for articular cartilage repair and regeneration. *Advanced Functional Materials*, 33(10):2212561. https://doi.org/10.1002/adfm.202212561

Gui X, Peng Z, Song P, et al., 2023. 3D printing of personalized polylactic acid scaffold laden with GelMA/autologous auricle cartilage to promote ear reconstruction. *Bio-Design and Manufacturing*, 6:451-463. https://doi.org/10.1007/s42242-023-00242-6

Han G, Lee H, Kang JM, et al., 2023. 3D-printed NIR-responsive bullets as multifunctional nanodrug platforms for image-guided local chemo-photothermal therapy. *Chemical Engineering Journal*, 477:147083. https://doi.org/10.1016/j.cej.2023.147083

Hua YJ, Huo YY, Bai BS, et al., 2022. Fabrication of biphasic cartilage-bone integrated scaffolds based on tissue-specific

photo-crosslinkable acellular matrix hydrogels. *Materials Today Bio*, 17:100489. https://doi.org/10.1016/j.mtbio.2022.100489

Kim SY, Han G, Hwang DB, et al., 2021. Design and usability evaluations of a 3D-printed implantable drug delivery device for acute liver failure in preclinical settings. *Advanced Healthcare Materials*, 10(14):2100497. https://doi.org/10.1002/adhm.202100497

Kim YH, Kanczler JM, Lanham S, et al., 2024. Biofabrication of nano-composite-based scaffolds containing human bone extracellular matrix for the differentiation of skeletal stem and progenitor cells. *Bio-Design and Manufacturing*, 7: 121-136. https://doi.org/10.1007/s42242-023-00265-z

Kwon H, Brown WE, Lee CA, et al., 2019. Surgical and tissue engineering strategies for articular cartilage and meniscus repair. *Nature Reviews Rheumatology*, 15(9):550-570. https://doi.org/10.1038/s41584-019-0255-1

Levingstone TJ, Ramesh A, Brady RT, et al., 2016a. Cell-free multi-layered collagen-based scaffolds demonstrate layer specific regeneration of functional osteochondral tissue in caprine joints. *Biomaterials*, 87:69-81. https://doi.org/10.1016/j.biomaterials.2016.02.006

Levingstone TJ, Thompson E, Matsiko A, et al., 2016b. Multi-layered collagen-based scaffolds for osteochondral defect repair in rabbits. *Acta Biomaterialia*, 32:149-160. https://doi.org/10.1016/j.actbio.2015.12.034

Li XS, Zhao Y, Zhao C, 2021. Applications of capillary action in drug delivery. *iScience*, 24(7):102810. https://doi.org/10.1016/j.isci.2021.102810

Liu H, Cheng YL, Chen JJ, et al., 2018. Component effect of stem cell-loaded thermosensitive polypeptide hydrogels on cartilage repair. *Acta Biomaterialia*, 73:103-111. https://doi.org/10.1016/j.actbio.2018.04.035

Liu JX, Gao YL, Zhang GR, et al., 2019. Follow-up study on autogenous osteochondral transplantation for cartilage defect of knee joint. *China Journal of Orthopaedics and Traumatology*, 32(4):346-349 (in Chinese). https://doi.org/10.3969/j.issn.1003-0034.2019.04.010

Liu JY, Li L, Suo HR, et al., 2019. 3D printing of biomimetic multi-layered GelMA/nHA scaffold for osteochondral defect repair. *Materials & Design*, 171:107708. https://doi.org/10.1016/j.matdes.2019.107708

Malda J, Groll J, van Weeren PR, 2019. Rethinking articular cartilage regeneration based on a 250-year-old statement. *Nature Reviews Rheumatology*, 15(10):571-572. https://doi.org/10.1038/s41584-019-0278-7

Parisi C, Salvatore L, Veschini L, et al., 2020. Biomimetic gradient scaffold of collagen-hydroxyapatite for osteochondral regeneration. *Journal of Tissue Engineering*, 11: 2041731419896068. https://doi.org/10.1177/2041731419896068

Pattnaik A, Sanket AS, Pradhan S, et al., 2023. Designing of gradient scaffolds and their applications in tissue regeneration. *Biomaterials*, 296:122078. https://doi.org/10.1016/j.biomaterials.2023.122078

Schizas N, Savvidou O, Triantafyllopoulos I, et al., 2019. Adjuvant therapies for the enhancement of microfracture technique in cartilage repair. *Orthopedic Reviews*, 11(3):7950. https://doi.org/10.4081/or.2019.7950

Shen CY, Wang J, Li GF, et al., 2024. Boosting cartilage repair with silk fibroin-DNA hydrogel-based cartilage organoid precursor. *Bioactive Materials*, 35:429-444. https://doi.org/10.1016/j.bioactmat.2024.02.016

Singh AK, Pramanik K, Biswas A, 2024. Constructing a biofunctional-ized 3D-printed gelatin/sodium alginate/chitosan tri-polymer com-plex scaffold with improvised biological and mechanical properties for bone-tissue engineering. *Bio-Design and Manufacturing*, 7:57-73. https://doi.org/10.1007/s42242-023-00249-z

Soleymani M, Motiee ES, Karbasi S, et al., 2024. Evaluation of the effects of decellularized umbilical cord Wharton's Jelly ECM on polyhydroxy butyrate electrospun scaffolds: a new strategy for cartilage tissue engineering. *Materials Today Chemistry*, 39:102145. https://doi.org/10.1016/j.mtchem.2024.102145

Sun ZX, Bonassar LJ, Putnam D, 2020. Influence of block length on articular cartilage lubrication with a diblock bottle-brush copolymer. *ACS Applied Materials & Interfaces*, 12(1):330-337. https://doi.org/10.1021/acsami.9b18933

Wang MK, Wu Y, Li GF, et al., 2024. Articular cartilage repair biomaterials: strategies and applications. *Materials Today Bio*, 24:100948. https://doi.org/10.1016/j.mtbio.2024.100948

Wang WZ, Li H, Song P, et al., 2024. Photo-crosslinked integrated triphasic scaffolds with gradient composition and strength for osteochondral regeneration. *Journal of Materials Chemistry B*, 12(5):1271-1284. https://doi.org/10.1039/d3tb02031b

Wang Z, Wang X, Huang Y, et al., 2024. Cav3.3-mediated endochondral ossification in a three-dimensional bioprinted GelMA hydrogel. *Bio-Design and Manufacturing*, 7:983-999. https://doi.org/10.1007/s42242-024-00287-1

Yang HX, Zheng MJ, Zhang YY, et al., 2024. Enhanced angiogenesis in porous poly(ε-caprolactone) scaffolds fortified with methacrylated hyaluronic acid hydrogel after subcutaneous transplantation. *Biomaterials Translational*, 5(1): 59-68. https://doi.org/10.12336/biomatertransl.2024.01.006

Yang SH, Wu HM, Peng C, et al., 2024. From the microspheres to scaffolds: advances in polymer microsphere scaffolds for bone regeneration applications. *Biomaterials Translational*, 5(3):274-299. https://doi.org/10.12336/biomatertransl.2024.03.005

Zhang X, Yan ZH, Guan GT, et al., 2022. Polyethylene glycol diacrylate scaffold filled with cell-laden methacrylamide gelatin/alginate hydrogels used for cartilage repair. *Journal of Biomaterials Applications*, 36(6):1019-1032. https://doi.org/10.1177/08853282211044853

Zhang YB, Liu XC, Zeng LD, et al., 2019. Polymer fiber scaffolds for bone and cartilage tissue engineering. *Advanced Functional Materials*, 29(36):1903279. https://doi.org/10.1002/adfm.201903279

Zhou BT, Xu PS, Li XZ, et al., 2005. Determination of gallium citrate injection by UV/VIS spectrophotometry. *Central South Pharmacy*, 3(1):30-31 (in Chinese). https://doi.org/10.3969/j.issn.1672-2981.2005.01.014

Electronic supplementary materials

Tables S1–S15, Figs. S1–S11